2-1-2016

Effects of Intraframe Distortion on Measures of Cone Mosaic Geometry from Adaptive Optics Scanning Light Ophthalmoscopy

Robert F. Cooper
Marquette University

Yusufu N. Sulai
Medical College of Wisconsin

Adam M. Dubis
University College London

Toco Y.P. Chui
New York Eye and Ear Infirmary

Richard B. Rosen
New York Eye and Ear Infirmary

See next page for additional authors

Authors

Robert F. Cooper, Yusufu N. Sulai, Adam M. Dubis, Toco Y.P. Chui, Richard B. Rosen, Michel Michaelides, Alfredo Dubra, and Joseph Carroll

Article

Effects of Intraframe Distortion on Measures of Cone Mosaic Geometry from Adaptive Optics Scanning Light Ophthalmoscopy

Robert F. Cooper[1], Yusufu N. Sulai[2], Adam M. Dubis[3,4], Toco Y. Chui[5,6], Richard B. Rosen[5,6], Michel Michaelides[3,4], Alfredo Dubra[1,2,7,8], and Joseph Carroll[1,2,7,8]

[1] Biomedical Engineering, Marquette University, Milwaukee, WI, USA
[2] Ophthalmology, Medical College of Wisconsin, Milwaukee, WI, USA
[3] Institute of Ophthalmology, University College London, London, UK
[4] Moorfields Eye Hospital, London, UK
[5] New York Eye and Ear Infirmary of Mount Sinai, New York, NY, USA
[6] Department of Ophthalmology, Icahn School of Medicine at Mount Sinai, New York, NY, USA
[7] Cell Biology, Neurobiology and Anatomy, Medical College of Wisconsin, Milwaukee, WI, USA
[8] Biophysics, Medical College of Wisconsin, Milwaukee, WI, USA

Purpose: To characterize the effects of intraframe distortion due to involuntary eye motion on measures of cone mosaic geometry derived from adaptive optics scanning light ophthalmoscope (AOSLO) images.

Methods: We acquired AOSLO image sequences from 20 subjects at 1.0, 2.0, and 5.0° temporal from fixation. An expert grader manually selected 10 minimally distorted reference frames from each 150-frame sequence for subsequent registration. Cone mosaic geometry was measured in all registered images ($n = 600$) using multiple metrics, and the repeatability of these metrics was used to assess the impact of the distortions from each reference frame. In nine additional subjects, we compared AOSLO-derived measurements to those from adaptive optics (AO)-fundus images, which do not contain system-imposed intraframe distortions.

Results: We observed substantial variation across subjects in the repeatability of density (1.2%–8.7%), inter-cell distance (0.8%–4.6%), percentage of six-sided Voronoi cells (0.8%–10.6%), and Voronoi cell area regularity (VCAR) (1.2%–13.2%). The average of all metrics extracted from AOSLO images (with the exception of VCAR) was not significantly different than those derived from AO-fundus images, though there was variability between individual images.

Conclusions: Our data demonstrate that the intraframe distortion found in AOSLO images can affect the accuracy and repeatability of cone mosaic metrics. It may be possible to use multiple images from the same retinal area to approximate a "distortionless" image, though more work is needed to evaluate the feasibility of this approach.

Translational Relevance: Even in subjects with good fixation, images from AOSLOs contain intraframe distortions due to eye motion during scanning. The existence of these artifacts emphasizes the need for caution when interpreting results derived from scanning instruments.

Introduction

Adaptive optics (AO) ophthalmoscopy enables high-resolution imaging of the human retina in vivo.[1–5] AO was first incorporated to a custom fundus camera,[1] permitting the visualization of cone photoreceptors outside the foveal center.[1,2,6,7] More recently, AO was added to a confocal scanning laser ophthalmoscope (cSLO); enhancing the axial sectioning of cSLOs as well as providing high lateral resolution.[8] Similarly, adaptive optics scanning light ophthalmoscopes (AOSLOs) allow the visualization of smaller retinal structures,

including foveal cones[9–11] and rods.[10,12,13] AO can also be applied to optical coherence tomography (OCT), combining OCT's excellent axial resolution with the enhanced lateral resolution from AO. This enables the extraction of high-resolution volumetric data consisting of symmetric voxels ($3 \times 3 \times 3$ μm), and the visualization of weakly reflective structures in the retina.[5,14–19]

Regardless of the AO imaging modality used, analysis of images of the photoreceptor mosaic often includes extraction of measurements that describe the geometry of the cone mosaic.[6,7,10,20,21] However, in (point or line) scanning ophthalmoscopes, the image pixels are recorded sequentially, rather than simultaneously as in fundus ophthalmoscopes. Given the relatively low frame rate (<30 Hz) and the high magnification of current AO scanning ophthalmoscopes (~1°), even the involuntary eye motion of subjects with good fixation can cause substantial image distortion (local shear and compression/expansion). In AOSLO, distortions from eye motion (Fig. 1) can be mitigated by registration[22,23] and eye tracking[24,25] methods, in conjunction with the selection of a minimally distorted reference (or template) image. However, even an AOSLO image that appears distortionless may contain residual distortion (Figs. 1A, 1C, 1D), potentially compromising subsequent quantitative analysis of retinal structures.

Determining the effect of intraframe distortion on quantitative measurements of the cone mosaic is essential to understanding the precision of such measurements. Here we examined the effect of intraframe distortion on metrics of cone mosaic geometry derived from AOSLO images using two approaches. First, we evaluated the variability in image metrics obtained when utilizing 10 different reference frames (selected by a single expert observer) from within a single AOSLO image sequence to generate 10 final images for analysis. Second, we compared AOSLO-derived measurements to those from "distortionless" AO-fundus images of the same subject to assess the anatomical accuracy of AOSLO images. These data provide important insight into the sensitivity of AOSLO-derived image metrics that should be taken into consideration when making longitudinal measurements of the cone mosaic.

Methods

Human Subjects

This research followed the tenets of the Declaration of Helsinki, and was approved by the institutional research boards at the Medical College of Wisconsin (MCW), Marquette University, Moorfields Eye Hospital (MEH), and the New York Eye and Ear Infirmary (NYEEI). Twenty-nine subjects were recruited for this study (19 at MCW, five at MEH, and five at NYEEI). Subjects provided informed consent after the nature and possible consequences of the study were explained. Axial length measurements were obtained from each subject using an IOL Master (Carl Zeiss Meditec, Dublin, CA). To convert from image pixels to microns on the retina, we first acquired images of a Ronchi ruling positioned at the focal plane of a lens with a 19-mm focal length to determine the conversion between image pixels and degrees. An adjusted axial length method[26] was then used to approximate the retinal magnification factor (in microns/degree) and convert to micron/pixel.

Imaging the Photoreceptor Mosaic

Images of the photoreceptor mosaic were obtained from subjects using an AOSLO from three different sites (MCW, NYEEI, and MEH). Each AOSLO used the same previously described design,[4] which acquires images at a line rate of approximately 15 kHz and a frame rate of 16.6 Hz. Additionally, we obtained images using a newly constructed AO fundus camera (Fig. 2) with an $0.8° \times 1.8°$ rectangular field of view (FOV) imaged through a 7.7-mm pupil at the eye. Wavefront sensing was performed with a Shack-Hartmann sensor consisting of a Rolera-XR camera (QImaging, Surrey, British Columbia, Canada) and a 7.8-mm focal length lenslet array arranged in a square lattice with a 203-μm pitch (Adaptive Optics Associates, Cambridge, MA). The measured wavefront aberrations were corrected using a Hi-Speed DM97 deformable mirror (ALPAO S.A.S., Biviers, Grenoble, France) at 8 Hz. The pupil of the eye was relayed to the deformable mirror and Shack-Hartmann using afocal telescopes made of pairs of spherical mirrors (CVI Laser optics, Albuquerque, NM; JML Optical Industries, Inc., Rochester, NY). Each afocal telescope was folded off the plane to minimize astigmatism in both the retinal and pupil plane.[4,27] We used an 841-nm super luminescent diode (SLD) with a bandwidth of 14.1 nm for retinal illumination and a 790-nm SLD with a 14-nm bandwidth as the wavefront sensing beacon. To reduce the effect of speckle in the imaging path, light from the 841-nm source was scanned on the cornea using a resonant galvanometric optical scanner (Electro-Optical Products Corp., Fresh Meadows, NY). The back-scattered 841 nm
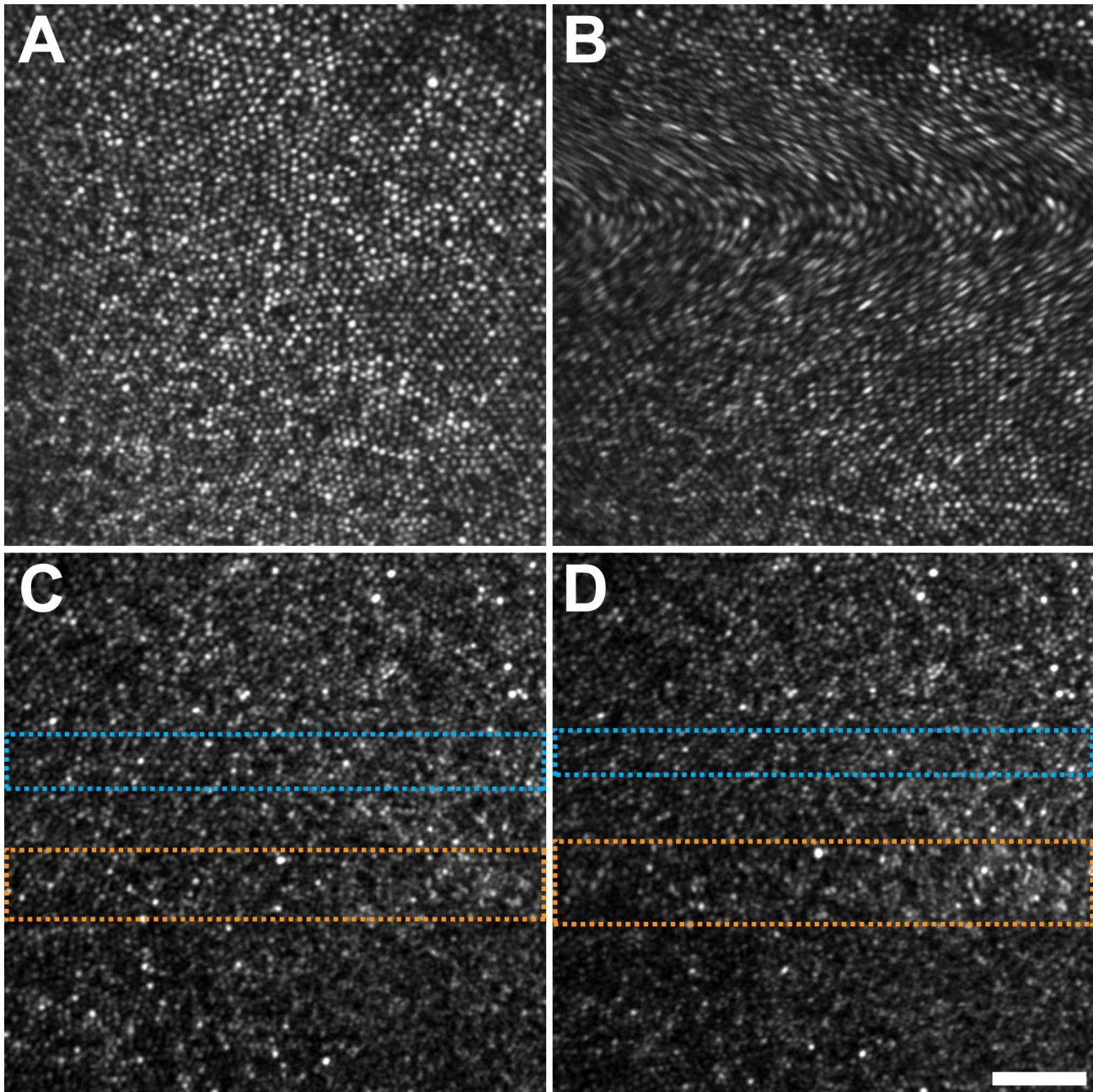
Figure 1. AOSLO images containing different quantities of distortion. AOSLO images in (A) and (B) are from the same retinal location; however, (A) was considered minimally distorted by an expert observer (RFC), while (B) contained too much distortion to be usable for analysis. While some forms of intraframe distortion are easily discernable, as between (A) and (B), this distortion is not always obvious. While the images in (C) and (D) were also considered minimally distorted reference frames, residual distortion could exist within either or both frames. This is depicted here as either a compression (*cyan box*), or expansion (*orange box*) of the image. *Scale bar* = 50 μm.

light was focused onto a Sarnoff CAM1M100-SFT (SRI International, Menlo Park, CA) 12-bit camera using a 400-mm focal length achromatic lens. Images were acquired using a 6-ms exposure. Custom image capture software was written using C++ in Windows 7 (Microsoft, Redmond, WA); a Qt-based (Digia, Helsinki, Finland) graphical user interface was created for acquisition control.

Static Image Distortion

In all AOSLO images, a sinusoidal static distortion was present in each image due to the properties of the
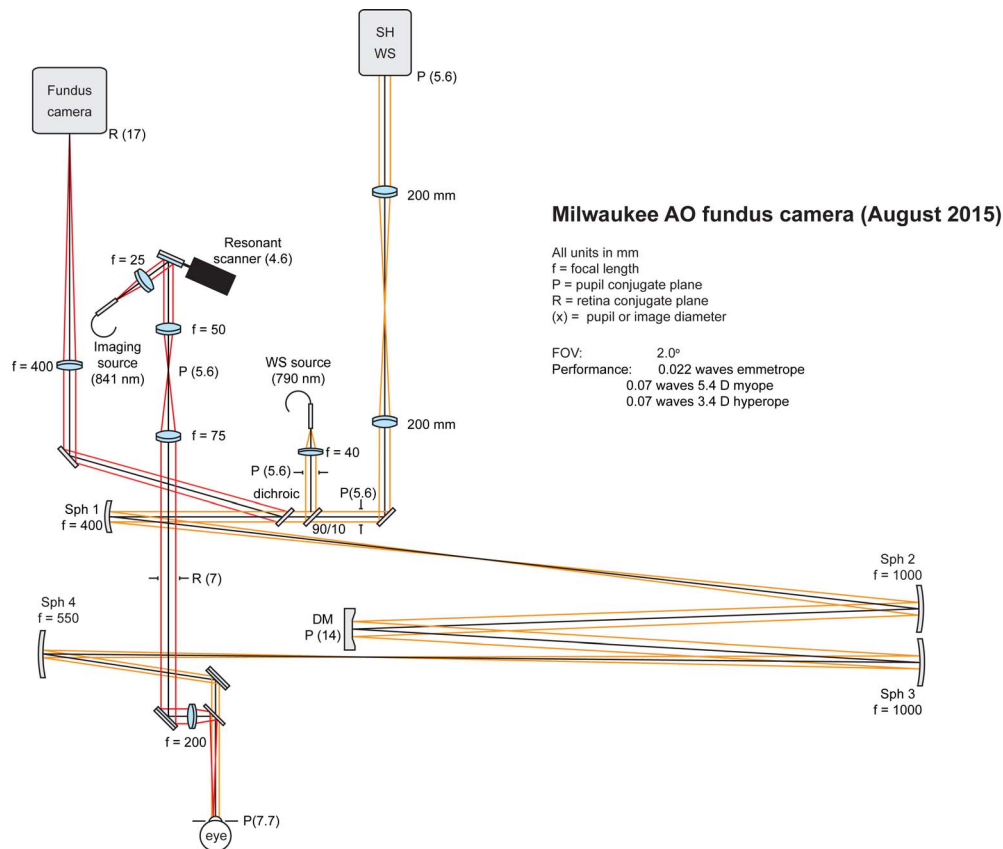
Figure 2. AO fundus camera system design. The schematic diagram of the AO fundus camera. DM, deformable mirror; RS, resonance scanner; SHWS, Shack-Hartmann wavefront sensor; Sph1-4, spherical mirrors; WS source, wavefront sensing source.

horizontal resonance scanner. This distortion was removed by estimating the image distortion from images of a stationary Ronchi ruling and then by resampling each frame of the raw image sequence over a grid of equally spaced pixels.[4,8]

To examine residual static distortion in both these "desinusoided" AOSLO images and the AO fundus images, we acquired images of a custom glass-embedded grid with 2-μm thick lines and an 8-μm pitch (Figs. 3A, 3C) by placing the grid at the focal plane of a model eye with a 19-mm focal length lens, and closed the AO loop to reduce residual system distortion. We then compared images of the grid to a derived ideal grid. We determined the center of each grid square using a previously defined semiautomatic cone counting algorithm.[28] To derive the ideal grid, we used the image grid coordinates contained from the central 5 × 5 grids to determine the average intergrid distance. An ideal coordinate grid with a pitch equivalent to the intergrid distance was created and aligned to the most central image grid square coordinates. Image grid and actual grid coordinates were paired by finding the nearest image grid

neighbor coordinate for each ideal coordinate. A heat map was created from the distance between each ideal and image coordinate pair (Figs. 3B, 3D). Overall distortion was defined as the root mean squared deviation from the perfect grid across all coordinates.

AOSLO Image Distortion from Eye Motion

To examine the distortion induced by normal involuntary microsaccades, image sequences consisting of 150 frames were obtained from 20 subjects at 1.0°, 2.0°, and 5.0° temporal (1T, 2T, and 5T) from the center of fixation. Within each sequence, a reference frame judged to have minimal intraframe distortion was selected by examining consecutive frame pairs that were translated relative to each other, and contained minimal stretching and compression. The remaining 149 frames were aligned to the reference frame using a previously described strip-registration method.[22] The 50 frames with the highest cross-correlation were averaged to produce a single image aligned to that reference frame. A total of 10 reference
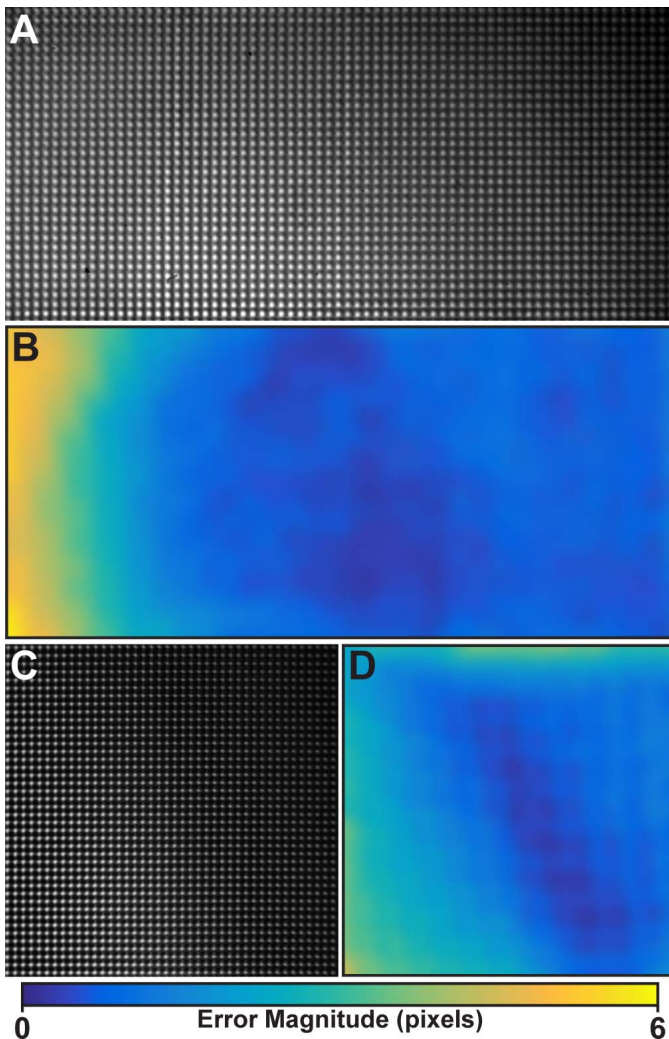
Figure 3. Static system distortion in AO fundus camera and AOSLO images. Images obtained of a two-dimensional grid using an AO fundus camera (A) and AOSLO (C) appear undistorted. However, residual distortions exist within each image; (B) and (D) illustrate the residual distortions that are present in the AO fundus image (B) and the AOSLO image (D). In order to correct these localized distortions, the images must be digitally resampled. Warmer colors correspond to high residual distortion (maximum: 6.1 pixels, or 0.01°), while cooler colors correspond to low residual distortion (minimum: 0 pixels).

frames were chosen in this manner for each AOSLO image sequence from each subject at each eccentricity, by a single expert observer (RFC). From the resultant 10 images, a *master* image containing the least visible distortion was selected, and the remaining nine *slave* images were coarsely aligned to this image by aligning them using the similarity transform in i2K Retina (DualAlign, LLC, Clifton Park, NY). All aligned images were cropped to 0.55 degrees. These cropped slave images were then finely aligned to the cropped

master image using strip-registration.[22] The strip-registration transformation applied to each image was recorded and converted to a pixel shift vector (PSV), which represented the x and y shifts applied to each row in each average image. This process is schematized in Supplementary Figure S1 (left and middle columns). Due to image stretching (Figs. 1C, 1D: orange box) and compression (Figs. 1C, 1D: cyan box), all 10 average images would rarely have PSVs for the top and bottom rows. Therefore, only PSVs from rows present in all 10 average images were included in the analysis. This resulted in a smaller analyzable area (~0.5°) across all subjects.

AOSLO Eye Motion Distortion Compared to AO Fundus Images

To further examine the distortion observed in AOSLO images, image sequences were obtained from nine additional subjects at 1T, 2T, and 5T from the center of fixation using both the AOSLO and the AO fundus camera at MCW. We processed the AOSLO image sequences as described above, resulting in 10 average images at each location for each subject. Each AO fundus image sequence had a flat-field correction applied to remove illumination nonuniformities.[2,29] Within each AO fundus image sequence, a reference frame with minimal motion blur was selected, and the remaining frames within the sequence were registered to the reference frame using cross correlation. The 80 frames with the highest correlation were averaged to create a single image for that AO fundus image sequence. The 10 average AOSLO images from each location were first manually aligned to the AO fundus image using Photoshop CS6 (Adobe, San Jose, CA). Each AOSLO image was cropped to 0.55°. To enable fine alignment, the image intensity in both the AOSLO and AO fundus images was normalized using local histogram equalization. The normalized AOSLO images were then registered to the normalized AO fundus image using strip-registration (Supplementary Video 1).[22] The transformation applied to each AOSLO image was recorded, and the transformations between each AOSLO image to the AO fundus image were converted to PSVs. This process is schematized in Supplementary Figure S2 (left and middle columns).

The Effect of Image Distortion on Cone Photoreceptor Metrics

To assess the effect of distortion on metrics of mosaic geometry, cone locations were identified

within each AOSLO master image or AO fundus image using a previously described semiautomated algorithm.[28] The cone coordinates for each average image were derived by transforming the master AOSLO image coordinates or AO fundus image coordinates to match each average image's distortion using the corresponding PSVs. For each subject, the cone coordinates from each image were cropped to the smallest common area from all images. The resultant coordinates were then analyzed using four measurements of photoreceptor arrangement: density, inter-cell distance (ICD), Voronoi cell area regularity (VCAR), and percentage of six-sided Voronoi regions. Density was calculated by first determining the Voronoi tessellation of the coordinates. Voronoi regions that extended outside the minimum and maximum and coordinates were considered *unbound* and excluded from the analysis. Voronoi cells contained within the minimum and maximum coordinates were considered *bound*. Density was determined by dividing the total number of bound Voronoi regions by the total bound Voronoi cell area. ICD was calculated by determining the average distance between all cells with bound Voronoi domains. VCAR was calculated by dividing the mean bound Voronoi cell area by the standard deviation of the bound Voronoi cell areas. The number of sides of each Voronoi cell was assessed to determine the percentage of six-sided Voronoi cells. It was also used to determine the percentage of Voronoi cells whose number of sides was conserved between each average image (AOSLO-only), or matched the AO fundus image (AOSLO/AO fundus comparison). To derive this, we created a Voronoi diagram for each image in a given image sequence, and determined the number of sides of each Voronoi cell in each image. We then created a histogram of each cell's number of sides through the image sequence, and used the histogram to determine which number of sides was the most common (AOSLO-only), or whether it matched the AO fundus image (AOSLO/AO fundus comparison). From these histograms, we calculated the percent conservation or percent matched. Additionally, in AOSLO-only image sequences, average PSV and repeatability statistics were calculated for each metric within each subject as previously described.[30] In AOSLO to AO fundus image comparisons, we determined the PSVs applied to each coordinate, and examined the coordinate shift and magnitude within each AOSLO/AO fundus image pair (Supplementary Video 1). In addition, we calculated the difference between the metrics derived from the

AO fundus image to the metrics from each AOSLO average image. These differences were then converted to relative percentages of the metrics derived from AO fundus image cone coordinates. The relative percentages across all subjects were compared to the AO fundus image's metrics using a one-sample Wilcoxon signed rank test. This process is outlined in Supplementary Figures S1 and S2 (right column).

Results

Static Image Distortion

The images of 2D grid patterns revealed that both the AOSLO and AO-fundus camera have small residual distortions at the edges of their $1° \times 1°$ and $0.8° \times 1.8°$ FOVs, respectively (Figs. 3A, 3C). In addition to the static distortions reported here, an affine distortion due to a misaligned slow scanner was present in the grid images from five of the subjects imaged in this study (JC_10549, JC_10567, JC_10418, AD_10302, JC_10620; Supplementary Fig. S3A). This distortion was due to a small misalignment in our AOSLO's slow scanner. To remove the shear distortion from the affected images, we created an ideal grid as described above and used coherent point drift[31] to register the image grid coordinates to the ideal coordinates. The affine transform used to register to the two point sets was then applied to the affected images to correct the image shear (Supplementary Fig. S3B). Interestingly, the majority of the distortion detected in the AO fundus image was on the left edge of the FOV (Fig. 3B), with a maximum of 6.1 pixels, or 0.01°, with a root mean square deviation of 1.9 pixels ($3.1° \times 10^{-3}$). In the AOSLO, distortion was also found around the edges of the FOV (Figs. 3B, 3D); however, it had a smaller maximum magnitude of 4.2 pixels, or $7.0° \times 10^{-3}$, and a root mean square deviation of 1.7 pixels ($2.8° \times 10^{-3}$). Despite the relatively high maximum deviations in both AOSLO and AO fundus camera, the vast majority of grid locations were close (<1 pixel, or $<1.6° \times 10^{-3}$) to the "ideal" 2D grid; this was reflected in the low root mean square deviation in both the AOSLO and AO fundus camera 2D grids.

The Effect of AOSLO Image Distortion on the Repeatability of Measures of Cone Mosaic Geometry

The PSV magnitudes in AOSLO were found to vary significantly within the images from each subject

Table 1. Interindividual and Intraretinal Variability in AOSLO Mean PSV Magnitude

	Mean ($\pm$ SD) PSV Magnitude (Pixels)		
Subject	1° Temporal	2° Temporal	5° Temporal
AD_10252	1.53 $\pm$ 0.94	1.55 $\pm$ 1.00	1.58 $\pm$ 0.91
AD_10253	1.17 $\pm$ 0.63	1.14 $\pm$ 0.61	1.39 $\pm$ 0.98
JC_0677	1.73 $\pm$ 0.97	1.08 $\pm$ 0.65	1.56 $\pm$ 1.08
JC_0878	1.65 $\pm$ 0.90	1.62 $\pm$ 1.39	2.44 $\pm$ 1.33
JC_10121	1.45 $\pm$ 0.78	1.56 $\pm$ 1.09	2.26 $\pm$ 1.51
JC_10122	1.14 $\pm$ 0.73	1.17 $\pm$ 0.65	1.08 $\pm$ 0.64
JC_10145	1.60 $\pm$ 0.97	1.72 $\pm$ 0.94	1.49 $\pm$ 1.01
JC_10304	1.32 $\pm$ 1.05	1.66 $\pm$ 1.01	1.42 $\pm$ 1.06
JC_10316	1.90 $\pm$ 1.07	1.75 $\pm$ 0.83	1.50 $\pm$ 0.84
JC_10318	3.42 $\pm$ 3.03	3.05 $\pm$ 1.52	1.78 $\pm$ 0.89
MM_0103	1.66 $\pm$ 1.25	1.16 $\pm$ 0.71	1.68 $\pm$ 1.00
MM_0136	1.43 $\pm$ 0.77	3.27 $\pm$ 1.33	3.51 $\pm$ 1.92
MM_0173	2.21 $\pm$ 1.39	2.28 $\pm$ 1.69	2.39 $\pm$ 1.31
MM_0182	1.52 $\pm$ 0.88	2.13 $\pm$ 1.24	2.27 $\pm$ 1.32
MM_0207	2.29 $\pm$ 1.43	1.95 $\pm$ 1.24	1.68 $\pm$ 1.03
RR_0025	1.11 $\pm$ 0.62	1.24 $\pm$ 0.76	0.97 $\pm$ 0.55
RR_0114	1.56 $\pm$ 0.99	1.57 $\pm$ 0.88	1.60 $\pm$ 0.93
RR_0358	1.45 $\pm$ 0.80	1.53 $\pm$ 1.16	1.25 $\pm$ 0.69
RR_0384	1.65 $\pm$ 0.87	1.55 $\pm$ 0.79	1.76 $\pm$ 1.05
RR_0424	1.63 $\pm$ 0.99	1.45 $\pm$ 0.76	1.37 $\pm$ 0.88
Average[a]	1.67 $\pm$ 1.16	1.72 $\pm$ 1.05	1.75 $\pm$ 1.09

[a] The average was defined as the mean of all subjects' PSV magnitudes $\pm$ the pooled standard deviation across all subjects' PSV magnitudes.

(two-way analysis of variance [ANOVA], $P < 0.001$). Average ($\pm$ standard deviation) PSV magnitudes ranged from as little as 0.97 $\pm$ 0.55 pixels ($1.6° \times 10^{-3} \pm 9.1° \times 10^{-4}$) to as much as 3.51 $\pm$ 1.92 pixels ($5.8° \times 10^{-3} \pm 3.1° \times 10^{-3}$; Table 1). The average PSV magnitude in AOSLOs did not vary significantly between MCW, NYEEI, and MEH (one-way ANOVA, $P = 0.54$). Upon examination of the effect of these distortions on the repeatability of metrics of photoreceptor structure (Table 2), we found that the mean ($\pm$ standard deviation) repeatability of density was 2.9 $\pm$ 1.2%, at 1T. Therefore, on average, the difference between two density measurements for the same subject would be less than 2.9% for 95% of pairs of observations. However, the repeatability varied from 1.1% to 7.3%; while the repeatabilities for most subjects were distributed tightly about the mean, the repeatabilities of some subjects were substantial outliers, contributing to the wider range. This property was mirrored in other metrics: ICD had a mean of 1.6% and a range of 0.8% to 3.2%,

percentage of six-sided Voronoi cells had a mean of 2.1% but a range of 0.8% to 4.6%, and VCAR had a mean of 7.5% and a range of 2.6% to 13.1%. Voronoi cell morphology was conserved in an average of 84.7% of Voronoi cells at 1T, implying that number of sides for 15.3% of Voronoi domains will change simply by using different reference frames. Interestingly, we determined that PSV magnitude was significantly correlated ($r = 0.73$; $P < 0.01$) with the repeatability of density, ICD, and the percentage of six-sided Voronoi cells, but not VCAR at 1T.

Interestingly, we found that the repeatability of each metric varied as a function of eccentricity (Fig. 4). On average, the repeatability of the cone density degrades with eccentricity, increasing from 2.9% $\pm$ 1.2% at 1T to 3.4% $\pm$ 1.4% and 3.9% $\pm$ 1.8% at 2T and 5T, respectively. Similarly, ICD's repeatability increased linearly, from 1.6% $\pm$ 0.54%, 1.7% $\pm$ 0.64%, and 2.0% $\pm$ 0.85% at 1T, 2T, and 5T, respectively. The repeatability of percent six-sided Voronoi cells was much lower at 1T (2.1% $\pm$ 1.1%) than at 2T and 5T

Table 2. Interindividual and Intraretinal Variability in Percent Repeatability for Four Cone Mosaic Metrics

Subject	1° Temporal				2° Temporal				5° Temporal			
	Density (%)	ICD (%)	% 6-Sided (%)	VCAR (%)	Density (%)	ICD (%)	% 6-Sided (%)	VCAR (%)	Density (%)	ICD (%)	% 6-Sided (%)	VCAR (%)
AD_10252	1.8	0.8	1.7	9.4	2.2	1.1	4.2	3.1	2.4	1.2	2.4	7.6
AD_10253	2.1	1.0	1.1	2.6	1.6	0.7	5.1	4.0	4.3	1.9	5.0	2.8
JC_0677	1.9	0.9	1.8	3.4	2.0	1.0	3.9	2.9	2.5	1.2	9.9	4.1
JC_0878	2.0	1.0	1.3	7.7	3.4	1.6	7.5	5.7	4.0	1.9	5.4	3.5
JC_10121	3.4	1.6	0.8	2.9	3.4	1.7	3.0	3.9	7.0	3.3	6.3	5.4
JC_10122	1.8	0.9	1.5	4.3	1.2	0.6	3.2	4.4	1.6	0.8	4.3	4.4
JC_10145	3.7	1.7	1.5	4.5	2.7	1.3	5.1	4.3	3.8	1.8	6.2	10.0
JC_10304	3.0	1.4	3.5	4.7	4.9	2.3	5.7	3.9	3.2	1.5	6.7	3.2
JC_10316	4.0	1.8	2.3	13.1	3.2	1.5	4.0	8.8	2.6	1.2	5.9	13.2
JC_10318	7.3	3.2	4.6	8.6	6.8	3.1	1.5	12.6	4.2	2.0	3.1	6.6
MM_0103	3.6	1.7	4.0	3.6	2.4	1.2	7.6	4.8	2.2	1.0	3.5	10.8
MM_0136	1.9	0.9	1.1	4.5	5.1	2.5	6.9	3.6	8.7	4.3	10.5	4.1
MM_0173	3.6	1.8	3.1	5.5	3.9	1.9	6.0	3.1	6.1	2.9	7.1	9.9
MM_0182	2.5	1.3	1.5	11.7	4.2	2.1	6.4	6.2	3.8	1.8	3.3	6.0
MM_0207	3.4	1.6	1.9	9.6	2.2	1.1	5.0	6.4	3.3	1.6	6.0	9.8
RR_0025	2.0	0.9	0.9	3.6	2.7	1.3	3.8	1.2	2.0	1.1	10.6	2.3
RR_0114	2.6	1.3	2.0	12.3	3.3	1.5	3.1	6.7	3.1	1.6	7.8	4.0
RR_0358	2.5	1.2	0.9	5.6	4.3	2.1	4.5	4.7	2.2	1.1	6.0	1.5
RR_0384	2.9	1.3	2.0	5.3	2.1	1.0	5.4	5.5	3.2	1.6	4.9	2.6
RR_0424	2.4	1.1	1.0	5.2	2.0	1.0	5.4	2.7	2.8	1.4	9.1	5.0
Average[a]	2.9	1.6	2.1	7.5	3.4	1.7	5.1	5.8	3.9	2.0	6.5	7.5

[a] The average repeatability was calculated using the pooled variance across all subjects.

(5.1% ± 1.6%, 6.5% ± 2.4%). VCAR's repeatability dropped from 7.5% ± 3.3% at 1T to 5.8% ± 2.5% at 2T, and rose again to 7.5% ± 3.3% at 5T. The conservation of Voronoi cell morphology also changed as a function of eccentricity; conservation decreased from the average of 84.7% at 1T to 71.6% and 73.2% at 2T and 5T (Fig. 5). Consistent with PSV magnitude at 1T, PSV magnitude was significantly correlated with density ($r = 0.62, 0.74$; $P < 0.01$) and ICD ($r = 0.63, 0.75$; $P < 0.01$) and uncorrelated with VCAR at 2T and 5T; however, the percentage of six-sided Voronoi cells was no longer correlated was uncorrelated at 2T and 5T.

The Effect of AOSLO Image Distortion on the Accuracy of Measures of Cone Mosaic Geometry

When examining the distortion in AOSLO images aligned to AO fundus images at 1T, we found that, on average, PSVs were Gaussian distributed with a mean (± standard deviation) of 0.27 ± 2.5 pixels along the x-axis, and 0.36 ± 2.4 pixels along the y-axis (Fig. 6C), with corresponding magnitudes of 1.84 ± 1.8 pixels along the x-axis and 1.79 ± 1.6 pixels along the y-axis. Similar to AOSLO-only PSVs, there was a wide range of AOSLO to AO fundus pixel shifts, ranging from as little as 0.06 ± 1.42 pixels ($9.9° \times 10^{-5} \pm 2.4° \times 10^{-3}$) to as much as 2.51 ± 6.71 pixels ($4.2° \times 10^{-3} \pm 1.1° \times 10^{-2}$). The PSVs were Gaussian distributed within a single subject (Fig. 6B), but not within a single AOSLO/AO fundus image pair (Fig. 6A). Other eccentricities followed similar patterns (Table 3).

We determined that both the density and ICD metrics from AOSLO images were not significantly different than AO fundus images (Figs. 7A, 7B) across all eccentricities ($P > 0.05$, Wilcoxon signed rank test). The percentage of six-sided cells calculated from AOSLO images was significantly different from
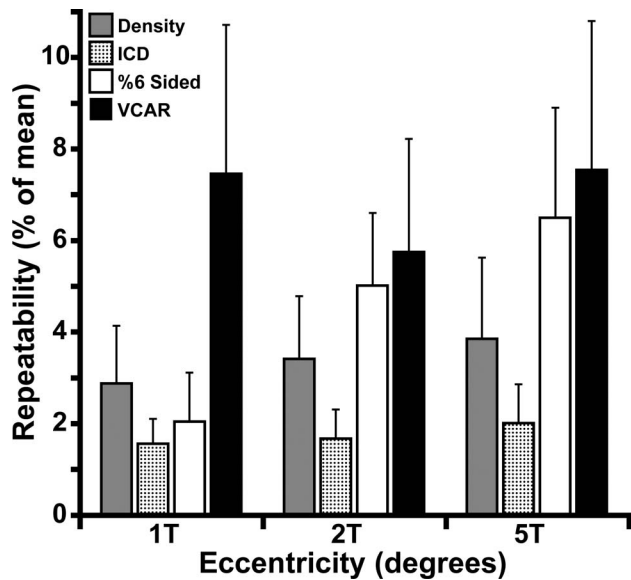
Figure 4. Repeatability as a function of eccentricity. Shown are the mean density (*gray fill*), ICD (*dotted fill*), percent six-sided Voronoi cells (*white fill*), and VCAR (*black fill*) with 1 SD error bars. The means of density and ICD increased similarly as a function of eccentricity. The mean of percent six-sided Voronoi cells increased dramatically from 1T to 2T, and more modestly from 2T to 5T. The mean of VCAR was the only metric that did not monotonically increase, showing better repeatability at 2T than at both 1T and 5T.

AO fundus images only at 1T ($P < 0.001$, Wilcoxon signed rank test; Fig. 7C). VCAR assessed in AOSLO images was significantly different than in AO fundus images for all examined eccentricities ($P < 0.001$, Wilcoxon signed rank test; Fig. 7D). On average, AOSLO number of Voronoi cell sides matched the flood frames in 77.7%, 74.9%, and 73.4% at 1T, 2T, and 5T, respectively (Fig. 8).

Discussion

After quantifying the static image distortion in both our AO ophthalmoscopes, we demonstrated that intraframe distortions due to involuntary eye motion and can affect the repeatability of measures of the cone mosaic in AOSLO images. In addition, by comparing AOSLO-derived measures to AO fundus camera images (which are relatively free of intraframe distortion), we showed that the accuracy can also be affected. These data demonstrate that distortion must be taken into consideration when interpreting metrics describing the cone mosaic using images obtained from scanning ophthalmoscopes. The approach outlined here could be used to evaluate the effect of distortions in other scanning ophthalmoscopes and
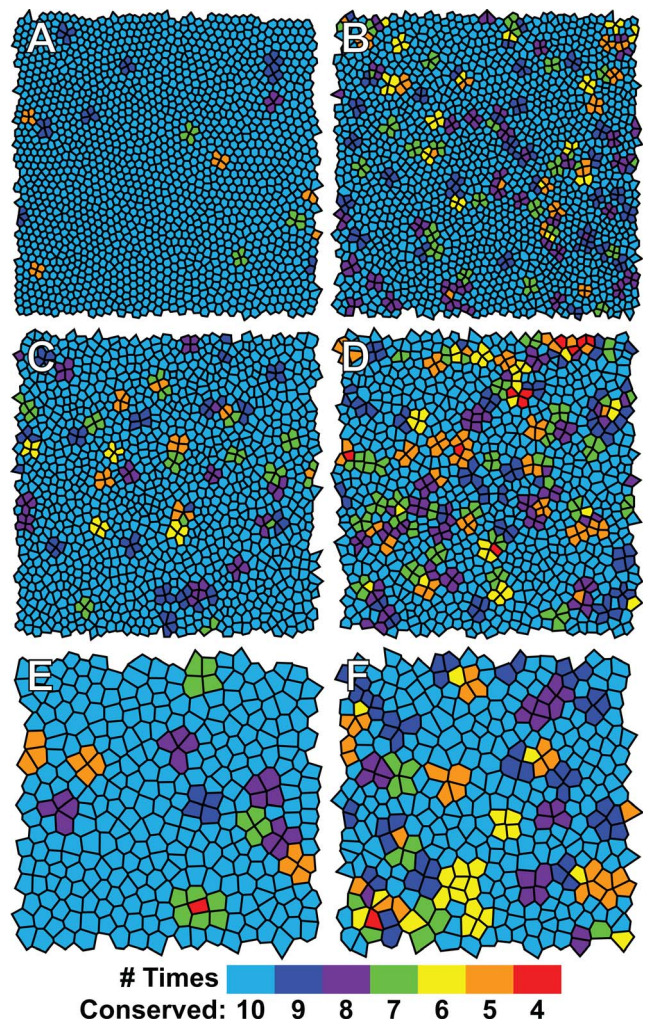
Figure 5. Conservation of Voronoi cell domain sides. Shown are Voronoi diagrams from exemplar AOSLO image sequences, illustrating conservation of cell domain sides across all 10 AOSLO frames. Each Voronoi cell is color-coded to indicate the maximum number of times that cell had the same number of sides across all average images. The *left column* shows ROIs that had a highly conserved number of Voronoi cell sides, and the *right column* shows ROIs with lower conservation. Each row corresponds to images obtained at 1° (A, B with 96.6% and 72.4% agreement, respectively), 2° (C, D with 80.7% and 58.3% agreement, respectively) or 5° (E, F with 82.0% and 58.5% agreement, respectively) temporal to fixation. The images from 1T generally had a higher percentage of percent six-sided cells than both 2T and 5T, potentially affecting the stability of the Voronoi map.

other cell mosaics such as the retinal pigment epithelium, as well as characterization of the shape/dimension of structures like blood vessels or nerve fiber layer bundles.

One limitation of our method is due to the image registration used in these analyses. The registration employs a strip-based rigid transform and assumes that


Figure 7. Relative photoreceptor measurement differences from AO fundus camera values. Shown are relative AOSLO values for density (A), ICD (B), percent six-sided Voronoi cells (C), and VCAR (D) at three different eccentricities. While there was generally good agreement, percent six-sided Voronoi cells and VCAR were significantly different ($P < 0.001$; asterisks) than the AO fundus camera. These differences suggest that VCAR and percent six-sided do not provide an accurate, but may provide a precise, estimate of the cone mosaic regularity.

It is important to emphasize that these findings apply only to the AOSLO systems used here (which had equivalent designs). It cannot be assumed that these results will be conserved between system designs, as the magnitude and variability of these distortions will vary between scanner types and optical components (Cooper et al. *IOVS*. 2013;54:ARVO E-Abstract 5546). Moreover, even slightly misaligned scanners can induce affine deformations of images produced from scanning ophthalmoscopes—until measuring it directly using the 2D grid (see Supplementary Fig. S3), we were completely unaware of such a misalignment in our system. Thus, not only must these distortions be measured experimentally across different systems, but they should be reassessed following any system alignment so they can be compensated for by digitally resampling each image. Our data highlight the need to conduct such an analysis prior to relying on measurements of the cone mosaic from a given point scanning-based device.

Additional factors could further limit the generalizability of these findings. For example, we examined repeatability at a fixed ROI size; however, it has been previously noted that the size of the ROI directly
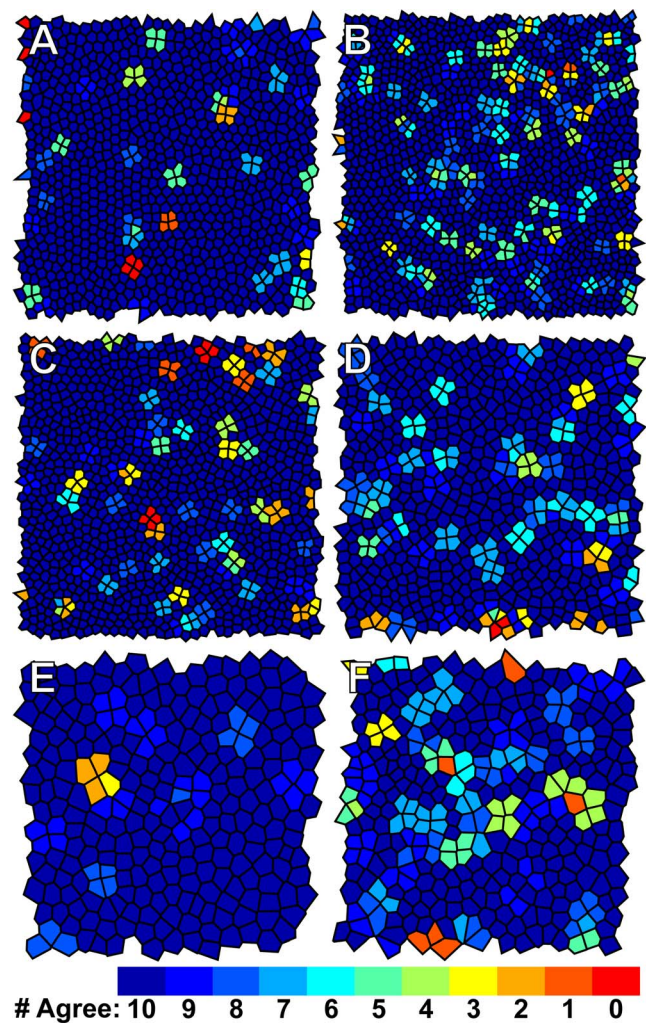
Figure 8. Agreement between AOSLO-derived Voronoi domains and AO fundus-derived Voronoi domains. Voronoi diagrams from exemplar AO fundus images showing the Voronoi cell domain agreement with respect to the corresponding aligned AOSLO average images. Each Voronoi cell is color-coded to indicate how many times the number of sides of the AO fundus derived Voronoi cell matched the number of sides of the Voronoi cell derived from the aligned AOSLO average images. The *left column* shows ROIs with a high amount of agreement to the AOSLO image sequences, and the *right column* shows ROIs with lower agreement. Data shown are from images acquired at 1° (A, B with 85.7% and 69.3% agreement, respectively), 2° (C, D with 81.4% and 70.3% agreement, respectively) or 5° (E, F with 88.2% and 59.4% agreement, respectively) temporal to fixation. Images corresponding to these maps may be found in Supplementary Figure S4.

influences both the metrics that are derived from a mosaic,[41] and their repeatability.[28] In addition, we observed that the repeatability of density, ICD, and percent six-sided cells was significantly linked to PSV magnitude (Tables 1 and 2). Therefore, in subjects

where increased image distortion is unavoidable (such as in subjects with nystagmus), one would expect the repeatability of the measurements to be worse.[42] Moreover, our data suggest that metrics such as density and ICD, which assess cones over an entire region of interest, respond differently to image distortion than metrics of local cone geometry (percent six-sided Voronoi regions and VCAR). This should be taken into account when choosing a metric for analysis of a given data set.

These data imply that the AOSLO distortions can, on average, be used to approximate a "distortionless" AO fundus image. This suggests that multiple AOSLO images could be aligned in order to achieve an accurate estimate of cone mosaic geometry without requiring an AO fundus camera. However, it is unlikely that 10 images (used here) would provide enough sampling of the PSV distribution to enable a consistently unbiased estimation of the AO fundus image; therefore, more images would be required to provide an accurate estimate of the true average distortion. Moreover, the manual selection of 10 co-localized frames from each AOSLO image sequence is impractical when data sets can consist of more than 100 image sequences. Thus, more efficient reference frame selection methods are needed to enable the creation of an average AOSLO image that accurately approximates an AO fundus image (i.e., the anatomical "truth").

In conclusion, we defined the effect of intraframe distortions due to involuntary intraframe eye movements on measurements of repeatability in subjects with good fixation. Moreover, we determined that a large, minimally distorted set of images acquired from our AOSLOs could be used to approximate "distortionless" AO fundus images. Characterizing both the static distortions and image distortions due to intraframe eye motion within each system and within multiple subject populations (especially those with unstable fixation and/or excessive eye motion) remains essential to the development of this modality as a clinical tool.

Acknowledgments

Disclosure: **R.F. Cooper**, None; **Y.N. Sulai**, None; **A.M. Dubis**, None; **T.Y. Chui**, None; **R.B. Rosen**, None; **M. Michaelides**, None; **A. Dubra**, None; **J. Carroll**, None

References

1. Liang J, Williams DR, Miller D. Supernormal vision and high-resolution retinal imaging through adaptive optics. *J Opt Soc Am A Opt Image Sci Vis*. 1997;14:2884–2892.
2. Bedggood P, Metha A. Variability in bleach kinetics and amount of photopigment between individual foveal cones. *Invest Ophthalmol Vis Sci*. 2012;53:3673–3681.
3. Roorda A, Garcia CA, Martin JA, et al. What can adaptive optics do for a scanning laser ophthalmoscope? *Bull Soc Belge Ophtalmol*. 2006;302:231–244.
4. Dubra A, Sulai Y. Reflective afocal broadband adaptive optics scanning ophthalmoscope. *Biomed Opt Express*. 2011;2:1757–1768.
5. Miller DT, Kocaoglu OP, Wang Q, Lee S. Adaptive optics and the eye (super resolution OCT). *Eye*. 2011;25:321–330.

6. Dees EW, Dubra A, Baraas RC. Variability in parafoveal cone mosaic in normal trichromatic individuals. *Biomed Opt Express*. 2011;2:1351–1358.

7. Baraas RC, Carroll J, Gunther KL, et al. Adaptive optics retinal imaging reveals S-cone dystrophy in tritan color-vision deficiency. *J Opt Soc Am A Opt Image Sci Vis*. 2007;24:1438–1447.

8. Roorda A, Romero-Borja F, Donnelly WJ, et al. Adaptive optics scanning laser ophthalmoscopy. *Opt Express*. 2002;10:405–412.

9. Zhang T, Godara, P, Blancob, ER, et al. Variability in human cone topography assessed by adaptive optics scanning laser ophthalmoscopy. *Am J Ophthalmol*. 2015;160:290–300.

10. Dubra A, Sulai Y, Norris JL, et al. Noninvasive imaging of the human rod photoreceptor mosaic using a confocal adaptive optics scanning ophthalmoscope. *Biomed Opt Express*. 2011;2:1864–1876.

11. Wilk MA, McAllister JT, Cooper RF, et al. Relationship between foveal cone specialization and pit morphology in albinism. *Invest Ophthalmol Vis Sci*. 2014;55:4186–4198.

12. Cooper RF, Dubis AM, Pavaskar A, Rha J, Dubra A, Carroll J. Spatial and temporal variation of rod photoreceptor reflectance in the human retina. *Biomed Opt Express*. 2011;2:2577–2589.

13. Merino D, Duncan JL, Tiruveedhula P, Roorda A. Observation of cone and rod photoreceptors in normal subjects and patients using a new generation adaptive optics scanning laser ophthalmoscope. *Biomed Opt Express*. 2011;2:2189–2201.

14. Hermann B, Fernández EJ, Unterhuber A, et al. Adaptive-optics ultrahigh-resolution optical coherence tomography. *Opt Lett*. 2004;29:2142–2144.

15. Zawadzki RJ, Cense B, Zhang Y, Choi SS, Miller DT, Werner JS. Ultrahigh-resolution optical coherence tomography with monochromatic and chromatic aberration correction. *Opt Express*. 2008;16:8126–8143.

16. Merino D, Dainty C, Bradu A, Podoleanu AG. Adaptive optics enhanced simultaneous *en-face* optical coherence tomography and scanning laser ophthalmoscopy. *Opt Express*. 2006;14:3345–3353.

17. Mujat M, Ferguson RD, Patel AH, Iftimia N, Lue N, Hammer DX. High resolution multimodal clinical ophthalmic imaging system. *Opt Express*. 2010;18:11607–11621.

18. Pircher M, Zawadzki RJ, Evans JW, Werner JS, Hitzenberger CK. Simultaneous imaging of human cone mosaic with adaptive optics enhanced scanning laser ophthalmoscopy and high-speed transversal scanning optical coherence tomography. *Opt Lett*. 2008;33:22–24.

19. Kocaoglu OP, Lee S, Jonnal RS, et al. Imaging cone photoreceptors in three dimensions and in time using ultrahigh resolution optical coherence tomography with adaptive optics. *Biomed Opt Express*. 2011;2:748–763.

20. Duncan JL, Zhang Y, Gandhi J, et al. High-resolution imaging with adaptive optics in patients with inherited retinal degeneration. *Invest Ophthalmol Vis Sci*. 2007;48:3283–3291.

21. Rossi EA, Chung M, Dubra A, Hunter JJ, Merigan WH, Williams DR. Imaging retinal mosaics in the living eye. *Eye*. 2011;25:1–8.

22. Dubra A, Harvey Z. Registration of 2D images from fast scanning ophthalmic instruments. In: Fischer B, Dawant B, Lorenz C, eds. *Lect Notes Comput Sc*: Springer Berlin / Heidelberg; 2010: 60–71.

23. Vogel CR, Arathorn DW, Roorda A, Parker A. Retinal motion estimation in adaptive optics scanning laser ophthalmoscopy. *Opt Express*. 2006;14:487–497.

24. Sheehy CK, Yang Q, Arathorn DW, Tiruveedhula P, de Boer JF, Roorda A. High-speed, image-based eye tracking with a scanning laser ophthalmoscope. *Biomed Opt Express*. 2012;3: 2611–2622.

25. Arathorn DW, Yang Q, Vogel CR, Zhang Y, Tiruveedhula P, Roorda A. Retinally stabilized cone-targeted stimulus delivery. *Opt Express*. 2007;15:13731–13744.

26. Bennett AG, Rudnicka AR, Edgar DF. Improvements on Littmann's method of determining the size of retinal features by fundus photography. *Graefes Arch Clin Exp Ophthalmol*. 1994;232:361–367.

27. Gómez-Vieyra A, Dubra A, Malacara-Hernández D, Williams DR. First-order design of off-axis reflective ophthalmic adaptive optics systems using afocal telescopes. *Opt Express*. 2009;17: 18906–18919.

28. Garrioch R, Langlo C, Dubis AM, Cooper RF, Dubra A, Carroll J. Repeatability of in vivo parafoveal cone density and spacing measurements. *Optom Vis Sci*. 2012;89:632–643.

29. Rha J, Schroeder B, Godara P, Carroll J. Variable optical activation of human cone photoreceptors visualized using short coherence light source. *Opt Lett*. 2009;34:3782–3784.

translational vision science & technology

30. Bland JM, Altman DG. Measuring agreement in method comparison studies. *Stat Methods Med Res*. 1999;8:135–160.

31. Myronenko ASX. Point-set registration: coherent point drift. *IEEE Trans Pattern Anal Mach Intell*. 2010;32:2262–2275.

32. Putnam NM, Hofer HJ, Doble N, Chen L, Carroll J, Williams DR. The locus of fixation and the foveal cone mosaic. *J Vis*. 2005;15:632–639.

33. Ramaswamy G, Devaney N. Pre-processing, registration and selection of adaptive optics corrected retinal images. *Ophthal Physl Opt*. 2013;33:527–539.

34. Pircher M, Kroisamer JS, Felberer F, Sattmann H, Götzinger E, Hitzenberger CK. Temporal changes of human cone photoreceptors observed in vivo with SLO/OCT. *Biomed Opt Express*. 2010;2:100–112.

35. Pallikaris A, Williams DR, Hofer H. The reflectance of single cones in the living human eye. *Invest Ophthalmol Vis Sci*. 2003;44:4580–4592.

36. Grieve K, Roorda A. Intrinsic signals from human cone photoreceptors. *Invest Ophthalmol Vis Sci*. 2008;49:713–719.

37. Wang Q, Tuten WS, Lujan BJ, et al. Adaptive optics microperimetry and OCT images show preserved function and recovery of cone visibility in macular telangiectasia type 2 retinal lesions. *Invest Ophthalmol Vis Sci*. 2015;56:778–786.

38. Liu B, Tarima S, Visotcky A, et al. The reliability of parafoveal cone density measurements. *Br J Ophthalmol*. 2014;98:1126–1131.

39. Metha A, Symons RC. Careful cone counting critical for clinical care. *Clin Experiment Ophthalmol*. 2014;42:807–809.

40. Bruce KS, Harmening WM, Langston BR, Tuten WS, Roorda A, Sincich LC. Normal perceptual sensitivity arising from weakly reflective cone photoreceptors. *Invest Ophthalmol Vis Sci*. 2015;56:4431–4438.

41. Lombardo M, Serrao S, Lombardo G. Technical factors influencing cone packing density estimates in adaptive optics flood illuminated retinal images. *PLoS One*. 2014;9:e107402.

42. Abozaid MA, Langlo CS, Dubis AM, Michaelides M, Tarima S, Carroll J. Reliability and repeatability of cone density measurements in patients with congenital achromatopsia. *Adv Exp Med Biol*. 2016;854:277–283.

translational vision science & technology